

HIGH-RESOLUTION NEAR-INFRARED SPECTROSCOPY OF AN EQUIVALENT WIDTH-SELECTED SAMPLE OF STARBURSTING DWARF GALAXIES

MICHAEL V. MASEDA¹, ARJEN VAN DER WEL¹, ELISABETE DA CUNHA¹, HANS-WALTER RIX¹, CAMILLA PACIFICI², IVELINA MOMCHEVA³, GABRIEL B. BRAMMER⁴, MARIJN FRANX⁵, PIETER VAN DOKKUM³, ERIC F. BELL⁶, HARRY C. FERGUSON⁷, MATTIA FUMAGALLI⁵, NORMAN A. GROGIN⁷, DALE D. KOCEVSKI⁸, ANTON M. KOEKEMOER⁷, BRITT F. LUNDGREN⁹, DANILO MARCHESINI¹⁰, ERICA J. NELSON³, SHANNON PATEL⁵, ROSALIND E. SKELTON¹¹, AMBER N. STRAUGHN¹², JONATHAN R. TRUMP³, BENJAMIN J. WEINER¹³, KATHERINE E. WHITAKER¹², STIJN WUYTS¹⁴

¹ Max-Planck-Institut für Astronomie, Königstuhl 17, D-69117 Heidelberg, Germany; email:maseda@mpia.de

² Yonsei University Observatory, Yonsei University, Seoul 120-749, Republic of Korea

³ Department of Astronomy, Yale University, New Haven, CT 06520, USA

⁴ European Southern Observatory, Alonso de Córdova 3107, Casilla 19001, Vitacura, Santiago, Chile

⁵ Leiden Observatory, Leiden University, Leiden, The Netherlands

⁶ Department of Astronomy, University of Michigan, 500 Church Street, Ann Arbor, MI 48109, USA

⁷ Space Telescope Science Institute, 3700 San Martin Drive, Baltimore, MD 21218, USA

⁸ University of California Observatories/Lick Observatory, University of California, Santa Cruz, CA 95064, USA

⁹ Department of Astronomy, University of Wisconsin, 475 N Charter Street, Madison, WI 53706, USA

¹⁰ Physics and Astronomy Department, Tufts University, Robinson Hall, Room 257, Medford, MA 02155, USA

¹¹ South African Astronomical Observatory, Observatory Road, Cape Town, South Africa

¹² Astrophysics Division, Goddard Space Flight Center, Code 665, Greenbelt, MD 20771, USA

¹³ Steward Observatory, 933 N. Cherry St., University of Arizona, Tucson, AZ 85721, USA and

¹⁴ Max-Planck-Institut für extraterrestrische Physik, Giessenbachstrasse 1, D-85748 Garching, Germany

Version: September 6, 2013

ABSTRACT

Spectroscopic observations from the *Large Binocular Telescope* and the *Very Large Telescope* reveal kinematically narrow lines ($\sim 50 \text{ km s}^{-1}$) for a sample of 14 Extreme Emission Line Galaxies (EELGs) at redshifts $1.4 < z < 2.3$. These measurements imply that the total dynamical masses of these systems are low ($\lesssim 3 \times 10^9 M_\odot$). Their large [O III]₅₀₀₇ equivalent widths (500 – 1100 Å) and faint blue continuum emission imply young ages of 10 – 100 Myr and stellar masses of $10^8 - 10^9 M_\odot$, confirming the presence of a violent starburst. The stellar mass formed in this vigorous starburst phase thus represents a large fraction of the total (dynamical) mass, without a significantly massive underlying population of older stars. The occurrence of such intense events in shallow potentials strongly suggests that supernova-driven winds must be of critical importance in the subsequent evolution of these systems.

Keywords: galaxies: dwarf — galaxies: evolution — galaxies: formation — galaxies: high-redshift — galaxies: starburst

1. INTRODUCTION

The $z > 1$ universe contains a remarkably large number of galaxies with extremely luminous nebular emission lines in comparison to their faint blue continua (van der Wel et al. 2011). These extreme emission line galaxies (EELGs) can have [O III] and/or H α equivalent widths (EWs) in excess of 500 Å (Atek et al. 2011; van der Wel et al. 2011; Brammer et al. 2012b). Such observations indicate that young starbursts dominate the energy output of these otherwise faint galaxies. While similar objects do exist at $z < 1$ (Cardamone et al. 2009; Izotov, Guseva, & Thuan 2011), they have much lower comoving number densities and thus their abundance must be a strong function of time.

More massive populations of older stars could easily be outshone by the young starbursts: an old stellar population could have mass-to-light ratios up to ~ 50 times larger than those of the bursts in the near-IR, so the main uncertainty in the interpretation of the observations hinges on the determination of the total masses of these systems. This missing datum prevents us from understanding the role of this mode of star formation in the broader context of galaxy formation: when these bursts occur in truly low-mass galaxies ($\sim 10^8 M_\odot$), the EELGs

may represent the main formation mode of present-day dwarf galaxies, as argued by van der Wel et al. (2011); alternatively, when these bursts occur in more massive systems ($\sim 10^9 M_\odot$) or at higher redshifts, we may be witnessing the early formation stage of Milky Way-type galaxies.

Dynamical mass estimates are key in addressing this issue. For this purpose we now present near-infrared spectroscopy of 14 EELGs at redshifts $1.4 < z < 2.3$ with [O III]₅₀₀₇ equivalent widths $> 500 \text{ Å}$ from the Large Binocular Telescope and the Very Large Telescope. In a companion paper (Maseda et al., in prep.; henceforth M13), we describe the observations and data reduction in full detail, as well as a more complete interpretation of the nature of these objects, while here we focus exclusively on their mass estimates. Besides the first dynamical mass measurements of such extreme galaxies, we also present improved total stellar mass estimates through stringent modeling of the continuum and emission line measurements from CANDELS multi-wavelength photometry (Grogin et al. 2011; Koekemoer et al. 2011) and low-resolution grism spectroscopy from the 3D-HST survey (Brammer et al. 2012a).

We adopt a flat Λ CDM cosmology with $\Omega_m = 0.3$ and

$H_0 = 70 \text{ km s}^{-1} \text{ Mpc}^{-1}$ throughout.

2. CANDIDATE SELECTION AND OBSERVATIONS

A full description of the sample selection, observations, and data reduction is given in M13. Here, we focus on the 14 objects¹⁵ with restframe equivalent widths $> 500 \text{ \AA}$ in $[\text{O III}]_{5007}$ from that emission line-selected sample: five are from the photometrically-selected sample of van der Wel et al. (2011) in the GOODS-S and UDS fields, one is from the grism sample of Straughn et al. (2011) in the GOODS-S field, and the remaining objects were selected based on their 3D-HST grism spectra in the COSMOS, GOODS-S, and UDS fields. Although the targets are very faint in the continuum ($m_{F140,AB} \gtrsim 24$), the emission lines are strong, with fluxes $> 10^{-17} \text{ erg s}^{-1} \text{ cm}^{-2} \text{ \AA}^{-1}$, making emission line detections possible with ~ 1 hour integrations on 8m class telescopes. We observe five objects using long-slit observations with the X-Shooter wide-band spectrograph (Vernet et al. 2011) at the *Very Large Telescope* from August to December 2012 (one slit contained two objects), focusing here on the combined $YJHK$ NIR region (1024–2480 nm), although it simultaneously observes in the UV-Blue and the Visible regions. Four had 40 minute integrations, while one object was observed for a total of 120 minutes in the near-IR over the course of two nights. The remaining ten objects in the sample were observed using the LUCI multi-object spectrograph (Seifert et al. 2003) at the *Large Binocular Telescope* with four separate masks between April 2012 and March 2013 in the J -, H -, and/or K -band (depending on the redshift, as we targeted $[\text{O III}]$ and/or $\text{H}\alpha$) for a minimum of 45 minutes per band. Not all targeted objects in the LUCI sample have detected emission lines, either due to their intrinsic faintness or contamination from OH skylines: in this case, two objects in the total sample had *a priori* equivalent widths greater than 500 \AA but severe contamination from OH skylines at the predicted position of the lines prevents a line extraction. For all observations, seeing was better than $1''$ and typically between $0.3''$ and $0.8''$. All exposures were dithered by $3''$ to decrease dependence on the pixel-to-pixel detector variations and defects.

Reduction of the X-Shooter data is performed using version 2.0.0 of the ESO XSHOOTER pipeline¹⁶, which provides merged, 2D near-IR spectra. Reduction of the LUCI data is performed using a custom pipeline, with the wavelength calibration done using the OH sky lines and based on the XIDL routines¹⁷. For the brightest emission lines, we also use XIDL for the final sky subtraction, which uses a spline-fitting algorithm to measure and remove the lines.

Identified emission lines in the 1D spectra are fit with Gaussian functions, where all lines in a subregion of the spectrum (i.e. $[\text{O III}] \lambda\lambda 4959, 5007$ and $\text{H}\beta$) are forced to

¹⁵ There are 15 objects in M13 that fulfill the equivalent width criteria. *COSMOS-10320*, although fulfilling the criteria, exhibits broad and asymmetric $[\text{O III}]$ (and also $\text{H}\alpha$) of $240 \pm 13 \text{ km s}^{-1}$. As this object is an obvious outlier (with a potential AGN contribution), we exclude it from the subsequent analysis and focus on the remaining 14 objects.

¹⁶ <http://www.eso.org/sci/software/pipelines/xshooter/xsh-pipe-recipes.html>

¹⁷ <http://www.icolick.org/~xavier/IDL/>

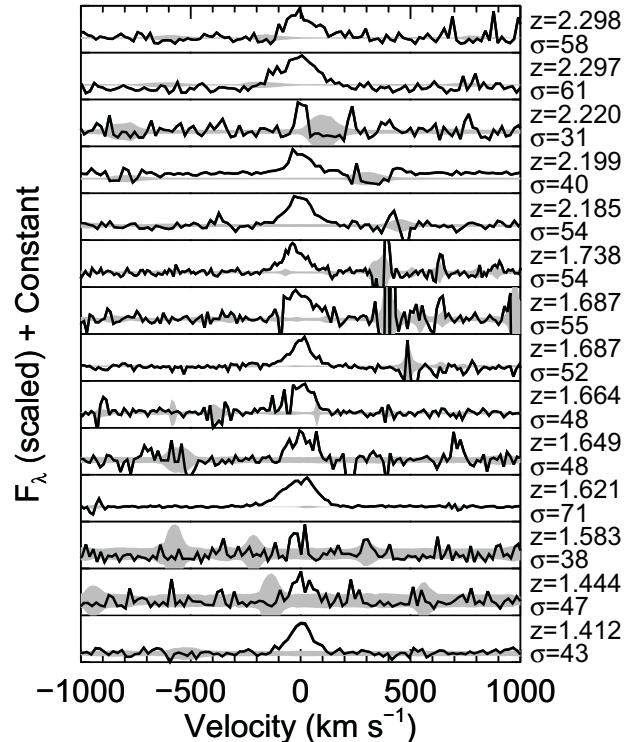


Figure 1. Plot of the $[\text{O III}]_{5007}$ emission line for each object in our sample, scaled to the peak flux value. Gray regions show the $\pm 1\text{-}\sigma$ flux uncertainties. Typical uncertainties are smaller than 10^{-4} in redshift and $\sim 8 \text{ km s}^{-1}$ in σ .

have the same width: only the ratio of the two $[\text{O III}]$ components is fixed to 2.98 (Storey & Zeippen 2000). When both $[\text{O III}]$ and $\text{H}\alpha$ are observed for a single object, we take the width of the higher-S/N line complex to be the “true” width, which is $[\text{O III}]$ for this entire sample. The two line widths are always consistent within $1\text{-}\sigma$.

Extracted emission lines are shown in Figure 1. The sample has a median line width of 48 km s^{-1} with an average uncertainty of 8 km s^{-1} , after correcting for seeing and instrumental broadening which is typically $\lesssim 20\%$ of the intrinsic line width.

3. DYNAMICAL AND STELLAR MASSES

3.1. Dynamical Mass Measurements

The velocity dispersions derived above can be used to estimate the dynamical masses according to:

$$M_{\text{dyn}} = C \frac{r_{\text{eff}} \sigma^2}{G}. \quad (1)$$

Here, we have adopted the half-light radius r_{eff} as the virial radius. We take r_{eff} as the half-light radius from van der Wel et al. (2012), who provide size measurements from the F125W and F160W HST/WFC3 CANDELS imaging. We choose the filter that does not contain the $[\text{O III}]$ emission line to ensure that the size is measured from the continuum light as much as possible. The typical r_{eff} is 1 kpc, which is larger than the HWHM of the PSF, so these sources are indeed resolved. As noted in Weiner et al. (2006), kinematic estimates using line widths yields a variety of results: Rix et al.

Table 1
Summary of Near-IR Observations and Masses

ID	RA (deg)	Dec (deg)	Instrument	z_{spec}	EW _{[OIII],5007} (Å)	$\sigma_{[OIII]}$ (km s ⁻¹)	M_{dyn} (M_{\odot})	M_* (MAGPHYS) (M_{\odot})
COSMOS-15144	150.156769	2.360800	LUCI1	1.412	1130±247	43.3±8.9	9.11±0.34	8.10 ^{+0.20} _{-0.26}
COSMOS-13848	150.176987	2.345390	LUCI1	1.444	888±351	46.7±14.4	9.22±0.40	8.58 ^{+0.14} _{-0.22}
COSMOS-12807	150.159546	2.333301	LUCI1	1.583	628±152	38.2±10.0	8.88±0.37	7.95 ^{+0.18} _{-0.24}
UDS-7444	34.473888	-5.234233	X-Shooter	1.621	713±42	71.1±5.7	9.66±0.33	8.78 ^{+0.07} _{-0.16}
COSMOS-16207	150.183090	2.372948	LUCI1	1.649	536±20	47.7±9.5	9.40±0.34	8.43 ^{+0.17} _{-0.12}
UDS-3760	34.428570	-5.255318	X-Shooter	1.664	731±86	48.2±5.9	9.04±0.31	7.98 ^{+0.11} _{-0.09}
UDS-3646	34.426483	-5.255770	X-Shooter	1.687	701±95	54.7±6.1	9.47±0.33	8.51 ^{+0.12} _{-0.13}
GOODS-S-17892	53.171936	-27.759146	X-Shooter	1.687	693±47	52.3±5.7	9.05±0.30	8.95 ^{+0.10} _{-0.11}
GOODS-S-26816	53.071293	-27.705803	X-Shooter	1.738	861±66	54.4±4.5 ^a	8.86±0.31	8.53 ^{+0.09} _{-0.11}
UDS-11484	34.431400	-5.212120	LUCI1	2.185	723±95	54.2±9.4	9.35±0.34	8.97 ^{+0.10} _{-0.12}
COSMOS-11212	150.124237	2.313672	LUCI1	2.199	598±189	40.3±8.9	8.78±0.36	8.77 ^{+0.23} _{-0.26}
COSMOS-8991	150.095352	2.287247	LUCI1	2.220	714±85	30.9±9.0	8.65±0.40	9.05 ^{+0.21} _{-0.27}
UDS-14655	34.391373	-5.195310	LUCI1	2.297	503±34	61.0±10.8	9.67±0.33	9.37 ^{+0.11} _{-0.31}
UDS-4501	34.390755	-5.250803	LUCI1	2.298	803±162	57.8±9.7	9.07±0.33	8.32 ^{+0.10} _{-0.19}

Note. — All IDs refer to the CANDELS catalog for that particular field (COSMOS, UDS, or GOODS-S), all equivalent widths are quoted in the restframe, and all masses are log quantities.

^a H α width.

(1997) calculate $C = 2.8$ for inclined rotating disks, while Barton & van Zee (2001) calculate $C = 2.1$ for blue compact dwarfs; Erb et al. (2006) use a simple geometric correction to obtain $C = 3.4$. Here we adopt $C = 3$, with a conservative uncertainty of 33%, as in Rix et al. (1997). Note that this value of C would be the same if we assume that these systems are spherical. We find that the 14 EELGs have $\log(M_{dyn}/M_{\odot})$ ranging from 8.7 to 9.7, with a median of 9.1 and an average uncertainty of 0.3.

Sources of systematic uncertainties in these estimates affect the results. First, the half-light radius is not necessarily equal to the virial radius, and some have irregular morphologies. Second, these systems likely have a more complicated dynamical structure. Third, and most importantly, the ionized gas in these systems is likely not virialized. Dynamical mass estimates on approximately kiloparsec scales, which we assume to be dominated by the baryonic content of these galaxies, are upper limits given our assumptions about the dynamics of these systems, namely since non-gravitational motion may significantly contribute to the measured velocity dispersion.

3.2. Stellar Mass Measurements

With confirmed redshifts, measured EWs of multiple lines, and multi-wavelength photometry, we are now in a position to estimate the stellar masses and improve upon the photometry-only method of van der Wel et al. (2011). We take 0.3–2.2 μ m photometry for the six objects in the GOODS-S field from Guo et al. (2013) and the three objects in the UDS field from Galametz et al. (2013): only six of the objects have uncontaminated IRAC Ch.1/2 fluxes, so for consistency we do not include them for any object, although the mass estimates are similar. No such multi-wavelength photometry is as of yet available for the six objects in the COSMOS field. For these objects we use CANDELS 4-band HST photometry (ACS F606W and F814W, WFC3 F125W and F160W).

We follow the procedure of van der Wel et al. (2011) to estimate ages and mass-to-light ratios (and hence stellar

masses) for the EELG sample based on photometrically-estimated H β EWs and the **Starburst99** model (SB99, Leitherer et al. 1999). This method assumes a constant star formation rate history and equal extinction of the emission lines and the continuum. The total EW is determined using the excess in F125W (F160W) compared to the continuum measured from F814W/F775W and F160 (F814W/F775W and F125), depending on the redshift. The EW is due to the combined effects of [O III] $\lambda\lambda 4959, 5007$ and H β ; we assume that H β contributes 1/8 of the combined EW. For the output burst age, the SB99 model predicts the (restframe) V -band mass-to-light ratio, which can be applied to the implied V -band luminosity determined from our J - or H -band observations, depending on the redshift of the object. Extinction is estimated by comparing the UV-continuum slopes of the SB99 model and the V/I -band ACS photometry, using the Calzetti et al. (2000) extinction law for starburst galaxies. Applying this method with continuous star formation, a Chabrier (2003) IMF, a high-mass cutoff of 100 M_{\odot} , and a metallicity of 0.2 Z_{\odot} , we derive burst masses in the range $\log(M/M_{\odot}) = 7.9 - 9.4$ for our sample of 14 EELGs.

With the additional data we have, we can use more sophisticated techniques to estimate stellar masses. Here we fit the broadband spectral energy distributions, including line fluxes measured from 3D-HST grism spectroscopy, of our galaxies using a custom version of the MAGPHYS code¹⁸ (da Cunha, Charlot, & Elbaz 2008) that includes nebular emission computed using the Pacifici et al. (2012) model (Charlot & Longhetti 2001, C. Pacifici et al., in prep.). The stellar emission is computed using the latest version of the Bruzual & Charlot (2003) models using a Chabrier (2003) IMF, and the attenuation by dust is accounted for using the two-component prescription of Charlot & Fall (2000). The nebular emission is computed using the CLOUDY photoionization code (Ferland 1996), as described in Pacifici et al. (2012).

¹⁸ <http://www.iap.fr/magphys/magphys/MAGPHYS.html>

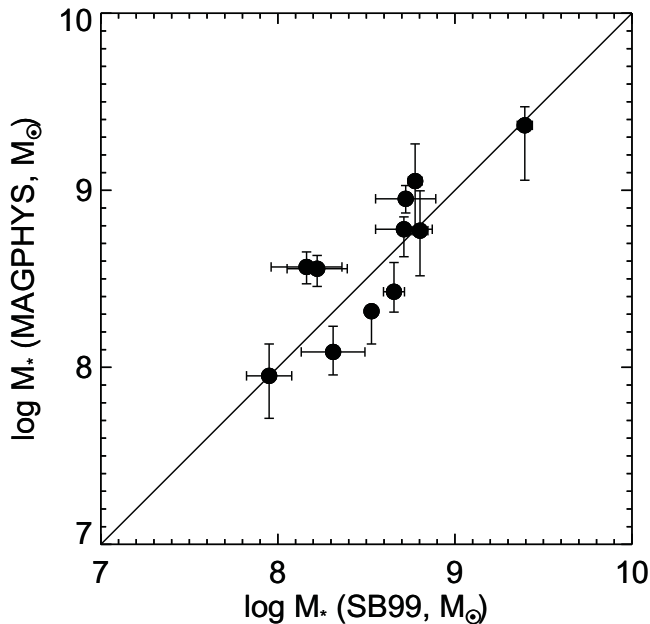


Figure 2. Comparison of MAGPHYS- and Starburst99-derived stellar masses for our sample. Starburst99 utilizes the equivalent width of $H\beta$ (determined from photometry alone) to calculate the masses, while MAGPHYS utilizes the full photometric SED and the emission line fluxes.

MAGPHYS uses a Bayesian approach to compare the measured photometry of observed galaxies with an extensive library of 100,000 spectral energy distribution models spanning a wide range in star formation histories, ages, and metallicities. The standard MAGPHYS priors (calibrated using more massive galaxies at low redshift) are not optimized for this specific population of young ages and low metallicities, so we have modified the standard priors to include a larger fraction of low metallicities (between 0.025 and $1 Z_{\odot}$), and younger ages by allowing both rising and declining star formation histories, all with superimposed random bursts of star formation. This method results in stellar masses in the range $\log(M/M_{\odot}) = 8.0 - 9.4$, which are listed in Table 1.

In Figure 2 we compare the SED-based stellar mass estimates with the photometric EW-based stellar mass estimates. The photometric method predicts values 1.1 times (0.05 dex) lower, with an intrinsic scatter (observed scatter minus the average uncertainty in the mass) of 0.20 dex, consistent with no systematic offset. The MAGPHYS modeling results reinforce the notion that these galaxies are dominated, in terms of stellar mass, by a very young stellar population. While the MAGPHYS modeling uses much more information, the crucial elements in both mass estimates are the blue continuum and the strong emission lines, which strongly constrain any modeling approach. Line and continuum luminosities, as well as dust content and metallicity, are comparable in the two models (see M13). Differences in population synthesis models leads to slight intrinsic differences in the M/L for a given age and metallicity. In addition, the photometric-EW method is very sensitive to the $H\beta$ equivalent width, which in this case is simply assumed from the photometry alone and does not utilize the additional spectroscopic $H\beta/[O III]$ information, also limiting its applicability to other redshifts. When the ratio is lower than the

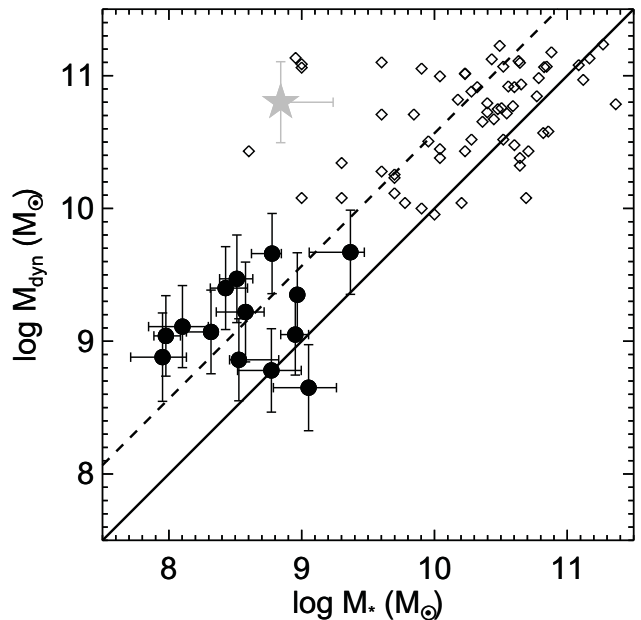


Figure 3. Dynamical masses determined from the velocity width of the emission lines versus stellar masses from the MAGPHYS SED fits to the full optical/near-IR SEDs for our equivalent width-selected sample. The dashed line shows the average value of 27.1% of the total dynamical mass made up by stars. The gray point is *COSMOS-10320*, which is not considered in the analysis. Open diamonds are from Erb et al. (2006) for star-forming galaxies at $z \sim 2$. Although the M_{dyn} values were derived in different manners (see Sec 3.1), the relationship between M_{dyn} and M_* is similar for the two samples.

$1/8$ as used in van der Wel et al. (2011), the resulting masses are higher. Finally, the simplistic assumptions of constant star formation and fixed metallicity, while applicable in general, lead to a very narrow range in ages of $\log(\text{age}/\text{yr}) = 6.8 - 7.4$: the older ages predicted by MAGPHYS are coupled with higher masses, where the oldest objects have the largest mass differences between the two methods. We thus deem the more rigorously-derived MAGPHYS masses to be more reliable.

Figure 3 compares the MAGPHYS stellar mass estimates with the dynamical estimates. $\log(M_{dyn}/M_*) = 0.57$ (27% of the total mass is in stars) ± 0.21 (random) ± 0.30 (sys) for the sample where the 0.30 dex systematic uncertainty is from the dynamical mass (see Section 2). The 0.21 dex random uncertainty contains the contributions from the measurement uncertainties and the limited sample size. The three points closest to the $M_{dyn} = M_*$ line illustrate the challenges to any modeling approach: two of them are the only $z \sim 2.2$ galaxies from the COSMOS sample, where the 4-band CANDELS photometry does not sample any continuum redward of $[O III]$, and the third is an object with two distinct components in the WFC3 imaging, where the assumptions contained in the dynamical mass estimate may not accurately reflect the true conditions in the system.

The low dynamical masses confirm the low-mass nature of these systems directly and exclude the presence of large amounts of unseen stars, gas, dust, or dark matter that exceed the observed amount of stellar matter by more than a factor of five. Our implied maximal gas fractions do not exceed those for more massive galaxies at similar redshifts, which range from $\sim 30 - 80\%$ (Daddi et al. 2010; Tacconi et al. 2013). As seen in Fig-

ure 3, our galaxies have similar M_{dyn}/M_* ratios to the starforming sample of Erb et al. (2006), albeit with EWs (and hence specific star formation rates) that are a factor of four higher. In M13 we further discuss the implications of our constraints under the assumption that the unseen matter is in the form of gas or dark matter.

4. CONCLUDING REMARKS

In this Letter we show kinematic line widths in the range $30 - 70 \text{ km s}^{-1}$ for a sample of 14 EELGs (with $\text{EW} > 500 \text{ \AA}$) at redshifts $1.4 < z < 2.3$. This constitutes the most comprehensive direct mass measurements for such low mass galaxies at these epochs. From this, we can now robustly conclude that these galaxies have low total masses ($\sim 10^{9.1} M_{\odot}$) and that the observed young starbursts ($\sim 10^{8.5} M_{\odot}$) constitute a substantial part of their total mass budget. These are not high-mass ($\gtrsim 10^{10} M_{\odot}$) galaxies: they do not contain a significant population of faint, older stars, and they do not have extremely high gas fractions. This confirms that the abundant population of EELGs at $z > 1$ constitute a common starburst phase among low-mass galaxies at these epochs given the duty cycle arguments presented in van der Wel et al. (2011). The wide range in observed stellar masses for a given equivalent width could indicate that these starbursts do not represent a homogeneous population but rather a phase in their evolution, given that the highest and lowest mass galaxies in this sample are potentially the progenitors of very different galaxies today. However, we could also be seeing a homogeneous population in which the scatter in mass is driven entirely by a scatter in age. A larger data set will help us to differentiate between the two scenarios.

Given the intensity of the starbursts and the shallow potential wells in which they occur, supernova-driven winds likely dominate the star formation history and subsequent evolution of these systems (Larson 1974). The starbursts may affect the central dark matter distribution (e.g. Navarro, Eke, & Frenk 1996; Read & Gilmore 2005; Pontzen & Governato 2012; Zolotov et al. 2012) and produce cored profiles that are commonly observed in present-day, low-mass galaxies. For a review see de Blok (2010), and Walker & Peñarrubia (2011); Amorisco & Evans (2012) for recent advances. Our current data set does not allow us to make stronger conclusions about the presence of feedback and winds via asymmetric or separate broad/narrow components in individual galaxies. However, with future spectroscopic studies of these objects, we will be able to search for such signals in stacked spectra.

In the present-day universe, such extreme starbursts are very rare (e.g. Cardamone et al. 2009), but at early epochs ($z > 4 - 6$) such events may well be the rule rather than the exception. It is becoming increasingly clear that strong emission lines affect the search for and interpretation of high- z galaxies. Strong emission lines galaxies at moderate redshifts ($z \sim 2$) can masquerade as drop-out selected $z > 10$ candidates (see discussion in e.g., Coe et al. 2013; Bouwens et al. 2013; Ellis et al. 2013; Brammer et al. 2013). Furthermore, for true high-redshift galaxies these strong emission lines are likely omnipresent (Smit et al. 2013) and affect the broad-band spectral energy distribution, so they should therefore be included in the modeling as de-

scribed here in Section 3.2 (also see Curtis-Lake et al. 2013; Schaerer, de Barros, & Sklias 2013). However, the results presented here are encouraging: we suggest that if strong emission lines are evident, then it is likely that the total stellar mass does not exceed by much that of the young stellar population traced by the blue continuum.

MVM is a member of the International Max Planck Research School for Astronomy and Cosmic Physics at the University of Heidelberg, IMPRS-HD, Germany. This work is based on observations taken by the 3D-HST Treasury Program and the CANDELS Multi-Cycle Treasury Program with the NASA/ESA HST, which is operated by the Association of Universities for Research in Astronomy, Inc., under NASA contract NAS5-26555, and at the European Southern Observatory, Chile, Program 089.B-0236(A).

Facilities: LBT, VLT:Melipal, HST.

REFERENCES

- Amorisco, N. C., & Evans, N. W. 2012, MNRAS, 419, 184
- Atek, H., Siana, B., Scarlata, C., et al. 2011, ApJ, 743, 121
- Barton, E. J., & van Zee, L. 2001, ApJ, 550L, 35
- Bouwens, R. J., Oesch, P. A., Illingworth, G. D., et al. 2013, ApJ, 765L, 16
- Brammer, G. B., van Dokkum, P. G., Franx, M., et al. 2012a, ApJS, 200, 13
- Brammer, G. B., Sánchez-Janssen, R., Labbé, I., et al. 2012b, ApJ, 758L, 17
- Brammer, G. B., van Dokkum, P. G., Illingworth, G. D., et al. 2013, ApJ, 765L, 2
- Bruzual, G., & Charlot, S. 2003, MNRAS, 344, 1000
- Calzetti, D., Armus, L., Bohlin, R. C., et al. 2000, ApJ, 533, 682
- Cardamone, C., Schawinski, K., Sarzi, M., et al. 2009, MNRAS, 399, 1191
- Chabrier, G. 2003, PASP, 115, 763
- Charlot, S., & Fall, S. M. 2000, ApJ, 539, 718
- Charlot, S., & Longhetti, M. 2001, MNRAS, 323, 887
- Coe, D., Zitrin, A., Carrasco, M., et al. 2013, ApJ, 762, 32
- Curtis-Lake, E., McLure, R. J., Dunlop, J. S., et al. 2013, MNRAS, 429, 302
- da Cunha, E., Charlot, S., & Elbaz, D. 2008, MNRAS, 388, 1595
- Daddi, E., Bournaud, F., Walter, F., et al. 2010, ApJ, 713, 686
- de Blok, W. J. G. 2010, Adv. Astron., article id. 789293
- Ellis, R. S., McLure, R. J., Dunlop, J. S., et al. 2013, ApJ, 763L, 7
- Erb, D. K., Steidel, C. C., Shapley, A. E., et al. 2006, ApJ, 646, 107
- Ferland, G. J. 1996, in Ferland, G. J., ed., Hazy, A Brief Introduction to Cloudy 90. Internal Report, Univ. Kentucky, Lexington
- Galametz, A., Grazian, A., Fontana, A., et al. 2013, ApJS, 206, 10
- Grogin, N., Kocevski, D., Faber, S., et al. 2011, ApJS, 197, 35
- Guo, Y., Ferguson, H. C., Gialvalisco, M., et al. 2013, ApJS, 207, 24
- Izotov, Y. I., Guseva, N. G., & Thuan, T. X. 2011, ApJ, 728, 161
- Koekemoer, A., Faber, S., Ferguson, H., et al. 2011, ApJS, 197, 36
- Larson, R. B., 1974, MNRAS, 169, 229
- Leitherer, C., Schaerer, D., Goldader, D., et al. 1999, ApJS, 123, 3
- Navarro, J., Eke, V., & Frenk, C., 1996, MNRAS, 283, 72
- Pacifici, C., Charlot, S., Blaizot, J., & Brinchmann, J. 2012, MNRAS, 421, 2002
- Pontzen, A., & Governato, F. 2012, MNRAS, 421, 3464
- Read, J. I., & Gilmore, G. 2005, MNRAS, 356, 107
- Rix, H.-W., Guhathakurta, P., Colless, M., & Ing, K. 1997, MNRAS, 285, 779
- Schaerer, D., de Barros, D., & Sklias, P. 2013, A&A, 549, 4
- Seifert, W., Appenzeller, I., Baumeister, H., et al. 2003, Proc. SPIE, 4841, 962
- Smit, R., Bouwens, R. J., Labbé, I., et al. 2013, arXiv:1307.5847
- Storey, P. J., & Zeppen, C. J. 2000, MNRAS, 312, 813
- Straughn, A. N., Kuntschner, H., Kümmel, M., et al. 2011, AJ, 141, 14

- Tacconi, L. J., Neri, R., Genzel, R., et al. 2013, ApJ, 768, 74
van der Wel, A., Straughn, A., Rix, H.-W., et al. 2011, ApJ, 742, 111
van der Wel, A., Bell, E., Haussler, B., et al. 2012, ApJS 203, 24
Vernet, J., Dekker, H., D'Odorico, S., et al. 2011, A&A, 536A, 105
Walker, M. G., & Peñarrubia, J. 2011, ApJ, 742, 20
Weiner, B. J., Willmer, C. N. A., Faber, S. M., et al. 2006, 653, 1027
Zolotov, A., Brooks, A. M., Willman, B., et al. 2012, ApJ, 761, 71